

PtCu thickness-modulated interfacial charge transfer and surface reactivity in stacked graphene/Pd@PtCu heterostructures for highly efficient visible-light reduction of CO₂ to CH₄

Yamin Xi ^{a,1}, Yue Zhang ^{b,1}, Xiaotong Cai ^{a,1}, Zhixin Fan ^a, Kefeng Wang ^a, Wenrou Dong ^a, Yue Shen ^a, Shuxian Zhong ^c, Li Yang ^{b,*}, Song Bai ^{a,*}

^a Key Laboratory of the Ministry of Education for Advanced Catalysis Materials, College of Chemistry and Life Sciences, Zhejiang Normal University, Jinhua, Zhejiang 321004, China

^b Institutes of Physical Science and Information Technology, Anhui University, Hefei 230601, China

^c College of Geography and Environmental Sciences, Zhejiang Normal University, Jinhua, Zhejiang 321004, China



ARTICLE INFO

Keywords:
Stacking design
Interfacial charge polarization
Photocatalysis
CO₂ reduction
Surface and interfacial engineering

ABSTRACT

Photocatalytic conversion of CO₂ to chemical feedstocks represents an intriguing approach to address the energy and environmental crisis, but faces low conversion efficiencies resulted from unsatisfied light absorption, charge recombination and surface reactivity of traditional semiconductor photocatalysts. Herein, we report stacked graphene/Pd@PtCu nanostructures with atomically thin PtCu shell to overcome above challenges and realize high-efficient CO₂-to-CH₄ photoreduction. The smart design begins with the excitation of Ru complex with broad visible absorption, which is followed by the smooth movement of photoelectrons via the graphene→Pd→PtCu pathway, and then the highly selective CO₂ reduction on the PtCu surface. As the PtCu thickness decreases, the strengthened Pd-PtCu interfacial charge polarization contributes to improved charge separation/migration. Meanwhile, CO₂ adsorption on the PtCu surface is ameliorated owing to increased electron accumulation and compressive strain. This work provides a new design for boosting the photocatalytic performance by cooperative surface and interfacial modulations.

1. Introduction

Solar driven conversion of redundant CO₂ molecules to valuable hydrocarbon fuels has emerged as an intriguing approach to simultaneously alleviate the energy crisis and circumvent the greenhouse effect [1–4]. Unfortunately, CO₂ photoreduction is an extremely difficult and complex process. On one hand, owing to the high dissociation energy of the C=O bond, the chemical transformation of CO₂ molecules suffers from low reactivity. On the other hand, multiple proton-coupled electron transfer reactions are involved in the CO₂ conversion process, which produce a wide variety of reduction products, such as CO (CO₂ + 2 H⁺ + 2 e⁻ → CO + H₂O), CH₃OH (CO₂ + 6 H⁺ + 6 e⁻ → CH₃OH + H₂O) and CH₄ (CO₂ + 8 H⁺ + 8 e⁻ → CH₄ + 2 H₂O) as well as H₂ from side H₂O reduction (2 H⁺ + 2 e⁻ → H₂) occurring simultaneously [5,6]. Resultantly, both the photocatalytic activity and selectivity are still far from fulfilling the industrial application requirements, which have yet to be

significantly improved.

Similar to other photocatalytic processes, CO₂ photoreduction primarily involves three essential steps: (i) light harvesting to generate photo-induced charge carriers, (ii) separation and transfer of charge carriers, and (iii) CO₂ reduction driven by the photoelectrons [7,8]. Generally, the CO₂ conversion efficiency mainly relies on the properties of photocatalysts in step i and ii, while step iii is closely related to the product distribution. Thus the optimization of the three steps and the balance of the thermodynamics and kinetics of them are highly desirable during the design of photocatalysts. Unfortunately, traditional semiconductor based photocatalysts often suffer from limited light absorption range, serious electron-hole recombination or sluggish surface reaction kinetics [9–12]. Firstly, resulted from the thermodynamic contradiction between optical absorption and redox potential, wide-band-gap semiconductors only absorb UV light accounting for a minor fraction of the solar spectrum, while narrow-band-gap

* Corresponding authors.

E-mail addresses: lyang@ahu.edu.cn (L. Yang), songbai@zjnu.edu.cn (S. Bai).

¹ These authors contributed equally to this work.

semiconductors extend the optical absorption to longer wavelength at the expense of its redox ability and exciton lifetime [13]. Secondly, photo-induced electrons and holes in semiconductors have a high probability of recombining with each other, resulting in the loss of majority of charge carriers in the bulk and on the surface prior to their participation in the redox reactions [14]. Thirdly, resulted from infertile reactive sites on the surface of semiconductors and high activation barrier of CO₂ molecules, surface reaction is usually the rate-determining step of the whole photocatalytic process, bottlenecking the eventual CO₂ conversion efficiency [15].

To simultaneously circumvent above issues, graphene based photocatalysts consisting of light sensitizers (e.g. Eosin Y and [Ru(bpy)₃]Cl₂) and cocatalysts (e.g. Pt, Co, MoS₂ and NiS_x) have been developed to substitute the traditional semiconductor based photocatalysts [16–19]. Generally, in the graphene based hybrid systems, molecular photosensitizers, owning a broad absorbance in visible range, act as light-harvesting components in donating photoelectrons [20]. Conductive graphene nanosheets adsorb the sensitizer molecules through π-π interaction, anchor the cocatalysts in preventing their aggregation or desorption, and provide high-speed channels for the migration of electrons from the sensitizers to cocatalysts [21]. Meanwhile, cocatalysts provide highly active and selective sites in modulating the adsorption/activation of the CO₂ molecules and manipulating the desorption of target products [22–24].

Similar to conventional semiconductor photocatalysts, rational surface and interface design of graphene based photocatalysts plays a vital role in improving the collaboration between different components and further boosting the catalytic efficiency [25–27]. On one hand, surface engineering on the supported cocatalysts should be performed to promote the forward reaction and simultaneously suppress the undesirable backward and side reactions based on the optimization of surface reactive sites. On the other hand, interfacial engineering between different components should be carried out to ensure the unidirectional and high-efficient transport of charge carriers and suppress the interfacial recombination losses. However, it is still a tough challenge to achieve simultaneous surface and interface design of graphene based photocatalysts [28,29]. In this paper, a unique stacking design of graphene/Pd@PtCu heterostructure has been demonstrated to overcome this limitation for highly active and selective photoreduction of CO₂ to CH₄ based on the rational construction of well-defined Pd@PtCu semi-core-shell nanostructure with tunable PtCu thickness. In this smart design, interfacial charge polarization, driven by the difference in the electronegativity between Pd cores and PtCu shells, promotes the interfacial electron transfer and enables more electron accumulation on the PtCu surface for 8-electron reduction of CO₂ to CH₄. Meanwhile, PtCu shells provide highly selective sites for the preferential transformation of CO₂ and H₂O to CH₄ as well as the suppression of side H₂ evolution. More importantly, with the shrinkage of the PtCu shell to atomic layer thickness, the increased electron density at the PtCu surface, together with the lattice strain resulting from the ultrathin coating, enhances the adsorption of reactive CO₂ molecules and further elevate the CO₂-to-CH₄ conversion efficiency.

2. Experimental

2.1. Synthesis of rGO/Pd@PtCu samples

In a typical synthesis of rGO/Pd@PtCu₂ L, 4.0 mL of rGO/Pd precursor (suspension concentration: 3.5 mg mL⁻¹ Pd in water), H₂PtCl₆·6H₂O (20 mg mL⁻¹, 0.5 mL in DMF), CuCl₂·2H₂O (6.583 mg mL⁻¹, 0.2 mL in DMF), PVP (K30, 200.0 mg), and 0.1 mL methylamine solution (30%) were mixed in 10 mL of DMF. The resulting homogeneous suspension was transferred to a Teflon-lined stainless steel autoclave with capacity of 15 mL and heated at 160 °C for 10.5 h. After the autoclave had cooled down to room temperature, the resultant product was separated by centrifugation, and washed with water and ethanol for

several times. For the synthesis of rGO/Pd@PtCu₆ L and rGO/Pd@PtCu₃₀ L, 1.0 and 0.2 mL suspensions of rGO/Pd precursors were used, respectively. Pd@Pt and Pd@PtCu core-shell nanocubes were prepared by following the same procedure of rGO/Pd@Pt and rGO/Pd@PtCu except the use of bare Pd instead of rGO/Pd as precursor.

2.2. Photocatalytic CO₂ reduction measurements

Photocatalytic CO₂ reduction tests were conducted in a sealed photocatalytic reactor (Beijing Perfectlight, China). In detail, 10 mg of photocatalysts and 15 mg of [Ru(bpy)₃]Cl₂·6H₂O were suspended in an acetonitrile/triethanolamine/H₂O solution (6 mL, 4:1:1, volume ratio), and dispersed on a flat glass plate at the bottom of the 100 mL photocatalytic reactor. The reactor was purged with high purity CO₂ for 30 min, and then irradiated by a 300 W Xe lamp (PLS-SXE300D/300DUV, Beijing Perfectlight, China) with visible light (420 < λ < 780 nm) as the illumination source, which was realized using a long-wave-pass cutoff filter with a cutoff wavelength of 420 nm and a short-wave-pass cutoff filter with a cutoff wavelength of 780 nm. The power density of the incident visible light reaching reaction solution was 100 mW cm⁻². The photocatalytic reaction was conducted for 4 h under stirring at 600 rpm. The evolved gaseous mixture was analyzed using a gas chromatograph (GC-2014, Shimadzu) with Ar as the carrier gas. The amount of H₂ was determined using a thermal conductivity detector (TCD). CH₄ was measured by a flame ionization detector (FID). CO was converted to CH₄ by using a methanation reactor and then analyzed by the FID. To detect the possible liquid reduction products such as CH₃OH and C₂H₅OH, the liquid supernatant was collected after the photocatalytic reaction and analyzed using a FID of gas chromatography (Agilent 8860). HCOOH is an exception, which was analyzed using a ¹H nuclear magnetic resonance (¹H NMR) spectrometer (Bruker Avance 600WB). The wavelength dependent photocatalytic performance was evaluated with the assistance of 365, 400, 450, 500 and 550 nm band-pass filters, respectively. During the cyclic tests, the catalyst was collected after each run and then reused for the next round of photocatalytic reaction. Isotope-labeling experiments were performed using ¹³CO₂ instead of ¹²CO₂ and the products were analyzed using gas chromatography-mass spectrometry (7890B/5977A, Agilent). The product selectivities were calculated according to the average evolution rates of the reduction products as well as the electrons required to generate products using the following equation:

$$\text{H}_2 \text{ selectivity} = 2v(\text{H}_2)/[2v(\text{H}_2) + 2v(\text{CO}) + 8v(\text{CH}_4)] \times 100\% \quad (1)$$

$$\text{CO selectivity} = 2v(\text{CO})/[2v(\text{H}_2) + 2v(\text{CO}) + 8v(\text{CH}_4)] \times 100\% \quad (2)$$

$$\text{CH}_4 \text{ selectivity} = 8v(\text{CH}_4)/[2v(\text{H}_2) + 2v(\text{CO}) + 8v(\text{CH}_4)] \times 100\% \quad (3)$$

where v(H₂), v(CO) and v(CH₄) stand for the formation rates of H₂, CO and CH₄, respectively, and 2, 2 and 8 electrons are required for H₂, CO and CH₄ production according to the above reaction equations.

2.3. Computational methods

All the geometric optimization and electronic simulation have been carried out by using the Vienna ab initio simulation package (VASP) [30]. The projector augmented-wave (PAW) method was chosen for the description of the core electrons [31]. The generalized gradient approximation-Perdew-Burke-Ernzerhof (GGA-PBE) exchange correlation functional was employed to perform the density functional theory computations [32]. An energy cutoff of 450 eV was adopted for the plane-wave expansion of the electronic wave function. The force and energy convergence criterion was set to be -0.02 eV/Å and 10⁻⁵ eV, respectively. A system of 2 × 2 slab with 1–4 layers was employed to model the PtCu surfaces while a system of 3 × 3 slab with 4 layers was employed to model the Pd surfaces. One bottom layer was fixed to the bulk positions with a vacuum space of 15 Å. The gamma-centered

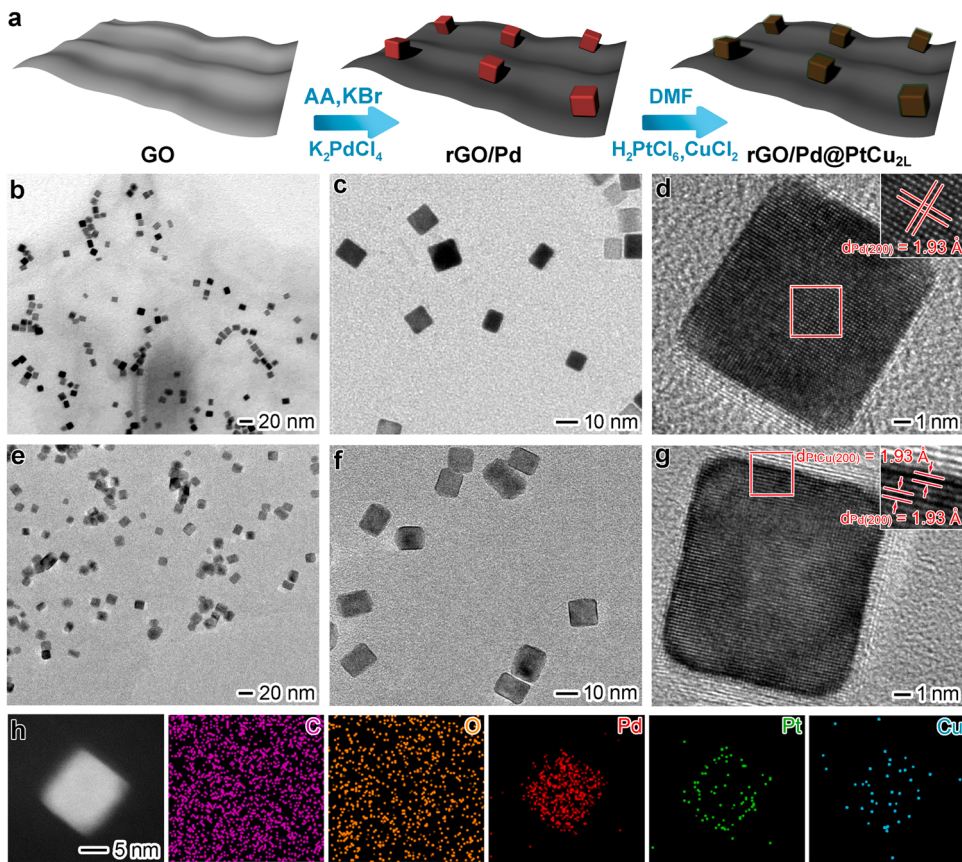


Fig. 1. Synthesis and electronic microscopy characterizations of rGO/Pd@PtCu with ultrathin PtCu shell: (a) schematic illustrating the synthesis of rGO/Pd@PtCu₂L; (b–g) TEM and HRTEM images of (b–d) rGO/Pd precursor and (e–g) rGO/Pd@PtCu₂L; (h) HAADF-STEM image and corresponding EDS mapping profiles of rGO/Pd@PtCu₂L.

k-point mesh of $3 \times 3 \times 1$ was used for the k-points sampling of the periodic geometries.

The adsorption energy (E_{ad}) of H₂O and CO₂ molecules on PtCu (100), Pt(100) and Pd(100) surfaces were calculated by the following equations:

$$E_{adH_2O} = E_{H_2O+surface} - (E_{H_2O} + E_{surface}) \quad (4)$$

$$E_{adCO_2} = E_{CO_2+surface} - (E_{CO_2} + E_{surface}) \quad (5)$$

Wherein, $E_{H_2O+surface}$ and $E_{CO_2+surface}$ are the total energies of H₂O and CO₂ adsorbed on the PtCu₁₋₄L, Pt(100) and Pd(100) surfaces, respectively. $E_{surface}$ is the total energy of the optimized PtCu₁₋₄L, Pt(100) or Pd(100), while E_{H_2O} and E_{CO_2} are the isolated energies of H₂O and CO₂ in vacuum, respectively.

3. Results and discussion

3.1. Sample synthesis and characterization

As illustrated in Fig. 1a, the synthetic process of the stacked catalyst begins with the in situ growth of Pd nanocrystals on reduced graphene oxide (rGO) by co-reducing K₂PdCl₄ and exfoliated graphite oxide (GO) (Fig. S1) with ascorbic acid (AA) as the reductant and KBr as the facet-selective capping agent [33]. According to the transmission electron microscopy (TEM) images, Pd nanocrystals with well-defined cubic profiles and average edge length of 10.7 nm are uniformly distributed on the surface of rGO nanosheets to fabricate the rGO/Pd precursor (Figs. 1b,c and S2a). The continuous lattice fringes with a periodic spacing of 1.93 Å in the high-resolution TEM (HRTEM) image agree well with the {200} lattice spacing of face-centered cubic (fcc) Pd. The fringe

orientation in the HRTEM image implies that the monocrystalline Pd nanocubes are enclosed by (100) facets (Fig. 1d) [34]. Then ultrathin PtCu shells are selectively grown on the surface of Pd by simultaneous reduction of H₂PtCl₆ and CuCl₂ with DMF (Fig. 1a). As shown in Fig. 1e and f, the cubic profile of Pd nanocrystals is well inherited after the coating of PtCu outer layer. Given that one face of Pd nanocube is in intimate contact with rGO, only five faces are covered by ultrathin PtCu shell to form semi-core-shell Pd@PtCu nanostructures. No nanoparticle in other morphology was observed in the TEM images. Owing to the higher electron density of PtCu than that of Pd, an image contrast between the inner gray core and exterior black shell can be clearly observed in the TEM and HRTEM images (Fig. 1f,g). As can be seen from the HRTEM image, atomically thin PtCu shell with the same lattice spacing of 1.93 Å is also a piece of single crystal exposed with (100) facets, which is epitaxially grown on the surface of Pd via the formation of perfect Pd(100)–PtCu(100) interfaces with a highly ordered atomic arrangement (Fig. 1g). Based on statistical analysis over more than 500 particles, the average edge length of the Pd@PtCu nanocrystals increases by 0.8 nm in comparison with that of bare Pd (Fig. S2b), corresponding to two atomic layers of PtCu shells. Thus the as-synthesized ternary photocatalyst is denoted as rGO/Pd@PtCu₂L. The scanning TEM (STEM) image together with the corresponding energy dispersive spectroscopy (EDS) mapping profiles further confirms the cubic semi-core-shell structure consisting of Pd core and PtCu shell as well as the substrate containing C and O in the rGO/Pd@PtCu₂L (Fig. 1h).

As reference samples, two rGO/Pd@PtCu counterparts with thicker PtCu shell were also synthesized for comparison. As revealed by the TEM images in Fig. 2a,b,d and e, with the deposition of more Pt and Cu atoms onto the Pd surface, the cuboid shape of Pd@PtCu is well maintained except the increased thickness of black PtCu outer layers. According to

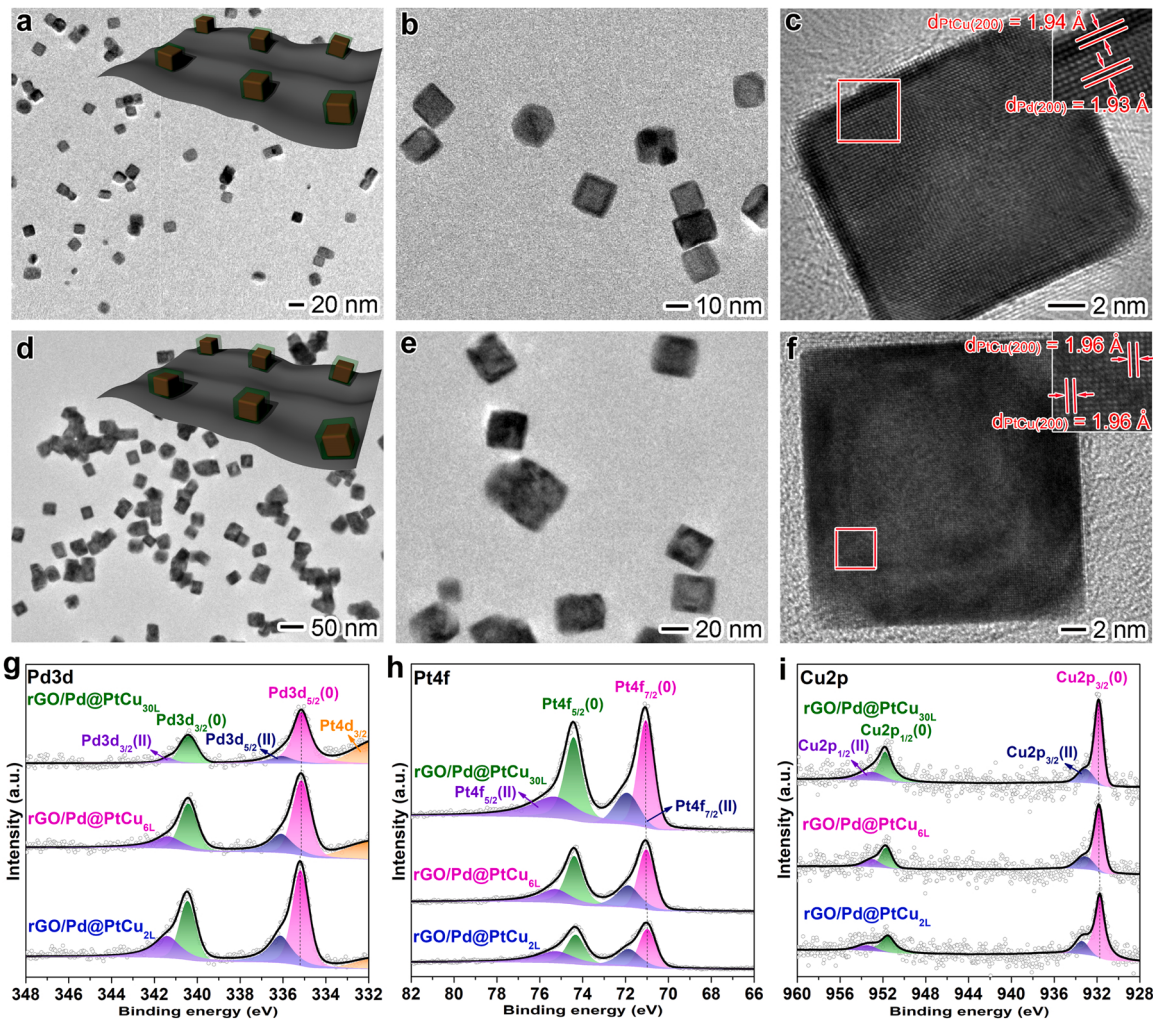


Fig. 2. Electronic microscopy characterizations of reference samples and comparative spectroscopic characterizations of rGO/Pd@PtCu_{2L} with reference samples: (a–f) TEM and HRTEM images of (a–c) rGO/Pd@PtCu_{6L} and (d–f) rGO/Pd@PtCu_{30L}; (g–i) high-resolution XPS spectra of rGO/Pd@PtCu samples: (g) Pd3d, (h) Pt4f and (i) Cu2p high-resolution spectrum.

the results of average edge length measurement, the thickness of PtCu is determined to be around 6 and 30 at. layers, and the corresponding sample is named as rGO/Pd@PtCu_{6L} and rGO/Pd@PtCu_{30L}, respectively (Fig. S2c,d). To further examine the PtCu shell thickness, the molar ratios of Pd to Pt and Cu were measured by inductively coupled plasma mass spectrometry (ICP-MS, Table S1), which turn out to be consistent with those determined by the size analyses. Moreover, the ICP-MS results indicate the approximate Pt/Cu molar ratio of around 70%: 30% in all the rGO/Pd@PtCu samples (Table S1). Similar to the case of rGO/Pd@PtCu_{2L}, both Pd(100) facet of the core and PtCu(100) facet of the shell can be observed in the HRTEM image of rGO/Pd@PtCu_{6L} (Fig. 2c). In sharp contrast, in the HRTEM image of rGO/Pd@PtCu_{30L}, due to the coverage of thicker shell, only the lattice of PtCu(100) plane can be detected (Fig. 2f). Furthermore, as the shell thickness increases, the lattice spacing of PtCu experiences a gradual increase from 1.93 Å of rGO/Pd@PtCu_{2L} to 1.94 Å of rGO/Pd@PtCu_{6L} and to 1.96 Å of rGO/Pd@PtCu_{30L}, which provides evidence that lattice mismatched epitaxy between Pd core and PtCu shell results in compressive strain on the ultrathin PtCu overlayers. When the shell thickness becomes greater, the strain gradually reduces and finally to the level of that of bulk PtCu [35–37].

The chemical states of the rGO/Pd@PtCu samples with different PtCu thicknesses were then comparatively analyzed by X-ray photoelectron spectroscopy (XPS). All the rGO/Pd@PtCu samples

demonstrate similar C1s and O1s signals, in which the higher peak intensity of sp² carbon (284.5 eV) relative to those of C–O (285.9 eV) and C=O (288.3 eV) groups implies the effective removal of oxygen-containing functional groups (Fig. S3) [38,39]. The deconvoluted peaks in the high-resolution spectra of Pd3d, Pt4f and Cu2p indicate the dominant metallic state and small amounts of ionic state, which are typical features for solution-synthesized metal nanocrystals (Fig. 2g–i) [40–44]. With the increasing PtCu thickness from rGO/Pd@PtCu_{2L} to rGO/Pd@PtCu_{6L} and to rGO/Pd@PtCu_{30L}, owing to the limited detection depth of XPS, Pt4f and Cu2p signals become stronger while Pd signal gradually weakens. Moreover, as the PtCu shell shrinks in the reverse order, Pd3d peaks shift to higher binding energies while Pt4f and Cu2p peaks to lower ones, suggesting that more significant charge re-distribution occurs between electron-deficient Pd cores and electron-rich PtCu shells.

In addition to above samples, other reference samples were also prepared for comparison. Bare rGO was obtained under the same experimental condition as rGO/Pd except the absence of K₂PdCl₄ (Fig. S4), while rGO/Pd@Pt_{6L} exposing with Pt(100) facets was synthesized through the same method as rGO/Pd@PtCu_{6L} except without the addition of CuCl₂ (Fig. S5). Bare Pd, Pd@Pt and Pd@PtCu core-shell nanocubes without rGO were also synthesized for comparison (Fig. S6). The structural information of the samples was revealed by the combination of X-ray diffraction (XRD) spectroscopy, Fourier-transform

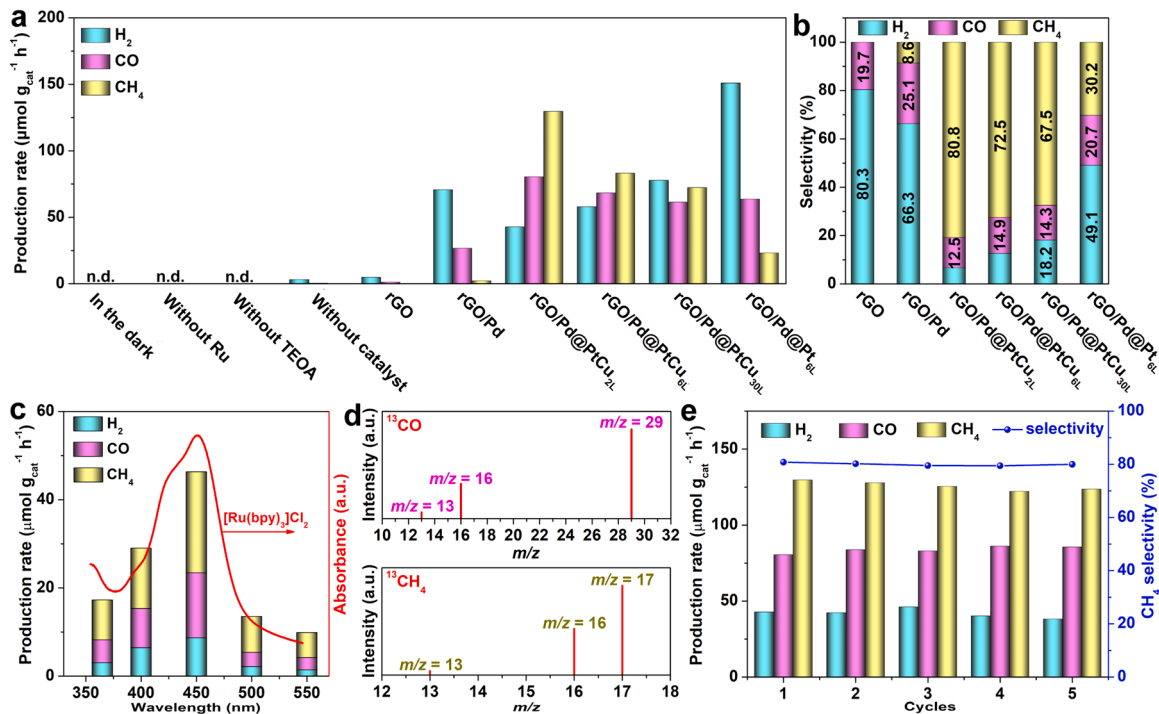


Fig. 3. Photocatalytic performance of rGO based catalysts under visible light irradiation: (a) comparison of the H_2 , CO and CH_4 production rates (n.d. is the abbreviation of “not detected”); (b) selectivities for H_2 , CO and CH_4 ; (c) wavelength-dependent H_2 , CO and CH_4 yields of rGO/Pd@PtCu_{2L} along with the light absorption spectrum of $[\text{Ru}(\text{bpy})_3]\text{Cl}_2$; (d) mass spectrum of ^{13}CO and $^{13}\text{CH}_4$ produced over rGO/Pd@PtCu_{2L}; (e) H_2 , CO and CH_4 production rates as well as the CH_4 selectivities over rGO/Pd@PtCu_{2L} in five successive cycles.

infrared (FTIR) spectroscopy and Raman spectroscopy. XRD patterns demonstrate the disappearance of the strong GO peak centered at $2\theta = 10.2^\circ$ in the rGO based samples, further proving the exfoliation and reduction of GO (Fig. S7) [45,46]. In addition to the broad peaks of rGO, all other peaks in the pattern of rGO/Pd can be assigned to fcc Pd (JCPDS 87–0639). With the further growth of PtCu on the Pd, no new peak appears, implying the same fcc phase of core and shell. As the PtCu thickness gradually increases from rGO/Pd@PtCu_{2L} to rGO/Pd@PtCu_{6L} and rGO/Pd@PtCu_{30L}, the intensity-enhanced metal peaks gradually shift towards those of standard Pt (JCPDS 65–2868) rather than Cu (JCPDS 01–1241), further indicating the majority of Pt and minority of Cu in the PtCu shell. Additionally, when compared with the XRD pattern of Pd@Pt, there is an obvious peak broadening of Pd@PtCu towards the direction of standard Cu (JCPDS 01–1241), and the peak broadening effect is more obvious at a higher 2θ value, further confirming the presence of Cu in the Pt lattice (Fig. S8) [47]. As depicted in the FTIR spectra of the rGO containing samples (Fig. S9), the remarkable decrease in the intensities of GO peaks corresponding to the stretching of oxygen containing functionalities including O-H (3400 cm^{-1}), C=O (1734 cm^{-1}), carboxy C-O (1400 cm^{-1}), epoxy C-O (1228 cm^{-1}) and alkoxy C-O (1065 cm^{-1}) further evidences the reduction of GO [48,49]. Such a phenomenon is further confirmed by the significant increase in the intensity ratio of D band to G band (I_D/I_G) in the Raman spectra, which is resulted from the presence of unpaired defects after the removal of oxygen-containing functional groups (Fig. S10) [50,51].

3.2. Photocatalytic performance analysis

Upon acquiring the structural and composition information, the performances of the rGO based samples in photocatalytic CO_2 reduction were evaluated with photosensitizer $[\text{Ru}(\text{bpy})_3]\text{Cl}_2$ as the light absorber and triethanolamine (TEOA) as the hole scavenger, respectively. Fig. 3a summarizes the catalytic performance of rGO/Pd@PtCu_{2L} in reference

to control samples under visible light irradiation ($420 < \lambda < 780 \text{ nm}$) in the first 4 h of reaction. For all the samples, the yields of reduction products gradually increase with the extension of the reaction time (Fig. S11). The corresponding product selectivity in Fig. 3b was calculated based on the average evolution rates of the reduction products as well as the electrons required to generate the products according to Eq. 1 ~ 3. No gas product was detected in the reference experiments including in the dark, without $[\text{Ru}(\text{bpy})_3]\text{Cl}_2$ and without TEOA. When the system was operated in absence of catalyst or in presence of rGO without metal anchored, trace amounts of H_2 and CO were detected. With the further combination of rGO with Pd, remarkable enhancements in the H_2 and CO evolution were observed along with the generation of trace amount of CH_4 . After the coating of Pd with ultrathin PtCu shell, the CH_4 production over rGO/Pd@PtCu_{2L} is drastically improved and the rate reaches up to as high as $129.7 \mu\text{mol g}^{-1} \text{h}^{-1}$, 56.4 times higher than that of rGO/Pd, offering high selectivity of 80.8% towards CH_4 production over competing H_2 and CO generation. Meanwhile, the H_2 and CO evolution rates also experience a considerable decline and rise, respectively, implying that the PtCu coverage facilitates the CO_2 fixation while suppresses the proton reduction. Further increasing the thickness of PtCu shell results in a gradual decrease in the CO and CH_4 production. Especially, the yield rate of CH_4 over rGO/Pd@PtCu_{6L} and rGO/Pd@PtCu_{30L} drastically decreases to 83.2 and $72.3 \mu\text{mol g}^{-1} \text{h}^{-1}$, while the corresponding CH_4 selectivity also suffers a slight drop to 72.5% and 67.5%, respectively, demonstrating the vital role of the PtCu thickness in the CO_2 -to- CH_4 conversion. In sharp contrast to rGO/Pd@PtCu_{2L}, with the approximate shell thickness, rGO/Pd@Pt_{6L} exhibits extremely higher H_2 generation but drastically lower CH_4 rate and selectivity, providing proof that the incorporation of Cu atoms into Pt surface holds the key to the high activity and selectivity of CH_4 production. It is worth noting that no liquid phase reduction product (e.g., CH_3OH and HCOOH) was detected for all the samples during the photocatalytic process. When Pd, Pd@Pt and Pd@PtCu without rGO were used as photocatalysts, no gas product was detected in the absence of $[\text{Ru}(\text{bpy})_3]\text{Cl}_2$.

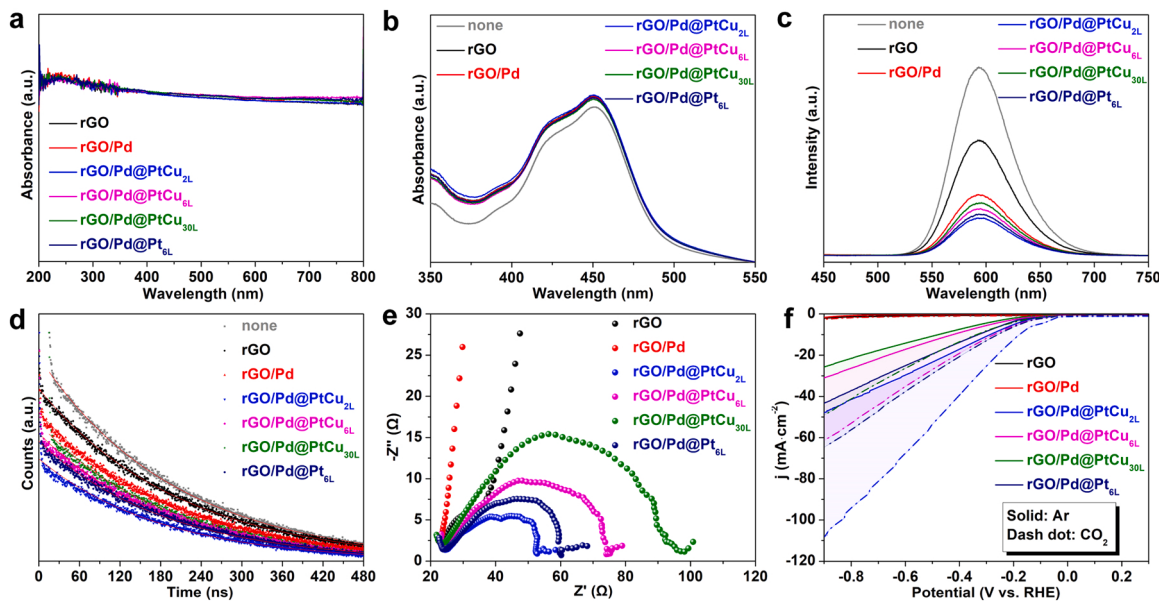


Fig. 4. Charge kinetics analyses of rGO based catalysts: (a) UV-vis diffuse reflectance spectra; (b) UV-vis absorption spectra of an aqueous solution containing 66 μM $[\text{Ru}(\text{bpy})_3]\text{Cl}_2$ in the presence of 100 μM rGO based catalysts; (c) steady-state PL spectra and (d) time-resolved PL decay spectra of an aqueous solution containing 66 μM $[\text{Ru}(\text{bpy})_3]\text{Cl}_2$ in the presence of 100- μM rGO based catalysts; (e) EIS Nyquist plots; (f) LSV curves recorded in Ar-saturated and CO_2 -saturated 0.5 M KHCO_3 .

(bpy)₃) Cl_2 , while trace amounts of H_2 and CO were measured in the presence of Ru complex, highlighting the pivotal role of rGO in the conversion of CO_2 to CH_4 (Fig. S12).

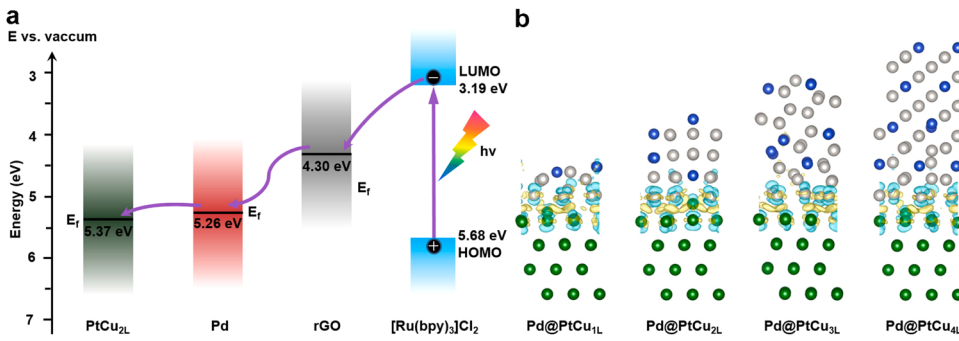
For rGO/Pd@PtCu_{2L} with the best photocatalytic performance, the activity and selectivity in CH_4 production are comparable to those of the reported state-of-the-art catalysts with $[\text{Ru}(\text{bpy})_3]\text{Cl}_2$ as the light sensitizer and TEOA as the hole scavenger, respectively (Table S2). To gain more information on the photocatalytic system, a series of control experiments with different reaction conditions have been conducted. The wavelength-dependent photocatalytic experiments was further assessed using Xe lamp equipped with different band filters. The trend of H_2 , CO and CH_4 yields of rGO/Pd@PtCu_{2L} at different wavelengths match well with light absorption profile of $[\text{Ru}(\text{bpy})_3]\text{Cl}_2$, corroborating that the CO_2 reduction is driven by the light excitation of the photosensitizer (Fig. 3c) [52]. When using Ar as the gas feedstock instead of CO_2 , no CO and CH_4 is detected, manifesting that the produced CO and CH_4 actually come from the reduction of CO_2 [53]. To further verify the origin of produced CO and CH_4 , the isotopic $^{13}\text{CO}_2$ was used as the reactant to trace the carbon source with rGO/Pd@PtCu_{2L} as a catalyst. As identified by gas chromatography-mass spectrometry (GC-MS), the strong signals at $m/z = 29$ and $m/z = 17$ corresponds to the generated ^{13}CO and $^{13}\text{CH}_4$, respectively, evincing that the CO and CH_4 indeed originate from the photoreduction of CO_2 (Fig. 3d) [54,55]. Noting that the $m/z = 16$ in the mass spectra does not correspond to $^{12}\text{CH}_4$, but the fragment ions of ^{13}CO and $^{13}\text{CH}_4$, respectively. Apart from high activity and selectivity, the rGO/Pd@PtCu_{2L} also delivers high catalytic stability in CH_4 generation. As shown in Fig. 3e, the recycled catalyst retain 95.3% of its original CH_4 evolution rate without obvious decay in the selectivity after five successive 4 h runs. To further prove the repeatability of the catalyst, TEM images, XRD pattern and XPS spectra after the cyclic tests were compared with those of the fresh one (Figs. S13 and S14). The well-maintained morphology, structure and composition validate the excellent reusability of the designed rGO/Pd@PtCu_{2L} catalyst in CO_2 photoreduction. Notably, after the cycles, the new emerging Ru3d peaks provide evidence that $[\text{Ru}(\text{bpy})_3]\text{Cl}_2$ is adsorbed on the rGO (Fig. S14b), while the attenuated peak intensities of oxygen-containing function groups in C1s and O1s spectra imply the deeper photoreduction of rGO nanosheets by transferred excited electrons from $[\text{Ru}(\text{bpy})_3]\text{Cl}_2$ light sensitizer (Fig. S14b,c) [17].

Furthermore, in comparison with the FTIR spectra of fresh rGO/Pd@PtCu_{2L}, additional absorption peaks at 775 cm^{-1} and 730 cm^{-1} after the photocatalytic cycles originate from the characteristic vibrations of adsorbed $[\text{Ru}(\text{bpy})_3]\text{Cl}_2$, confirming the π - π interaction between rGO and $[\text{Ru}(\text{bpy})_3]\text{Cl}_2$ (Fig. S15).

3.3. Photocatalytic mechanism analysis

To further explore the key factors determining the photocatalytic performance, UV-vis diffuse reflectance spectroscopy was firstly employed to examine the light absorption behaviors of the rGO based catalysts. As shown in Fig. 4a, all the samples exhibit comparable light absorption without obvious absorption edge, which is a typical feature for zero-bandgap graphene based materials. With the addition of the catalysts into $[\text{Ru}(\text{bpy})_3]\text{Cl}_2$ aqueous solution, there is a slight enhancement in the UV-vis absorption spectra (Fig. 4b). This enhancement is attributed to the intrinsic light absorption of rGO based catalysts, which can be reflected by the incremental light absorption of $[\text{Ru}(\text{bpy})_3]\text{Cl}_2$ upon the addition of increasing amounts of rGO/Pd@PtCu_{2L} (Fig. S16a). Owing to the comparable optical absorption property of the rGO based samples, almost no difference in the absorption spectra of $[\text{Ru}(\text{bpy})_3]\text{Cl}_2$ solution is observed in the presence of the same concentration of different samples, excluding the influence of the light absorption on the photocatalytic performance.

The charge separation and transfer behaviors in the rGO based samples were then reflected by steady-state photoluminescence (PL) spectroscopy. As sketched in Fig. 4c, $[\text{Ru}(\text{bpy})_3]\text{Cl}_2$ aqueous solution excited at 400 nm shows a strong emission peak around 610 nm. With the further addition of rGO based samples, the PL of the excited $[\text{Ru}(\text{bpy})_3]^{2+}$ is obviously quenched, and the quenching degree gradually increases with the increasing amount of rGO/Pd@PtCu_{2L} (Fig. S16b). The above result suggests the suppression of radiative charge recombination resulted from the transfer of photoexcited electrons from $[\text{Ru}(\text{bpy})_3]\text{Cl}_2$ light absorber to rGO based catalysts. With the same dosage of the catalysts, the PL quenching degrees are in the order: rGO < rGO/Pd < rGO/Pd@PtCu_{30L} < rGO/Pd@PtCu_{6L} < rGO/Pd@Pt_{6L} < rGO/Pd@PtCu_{2L}, signifying that the metal configuration on the rGO nanosheets is critical to the charge separation efficiency. When bare Pd nanocubes were added into the $[\text{Ru}(\text{bpy})_3]\text{Cl}_2$ solution in the absence of



rGO, no apparent PL quenching occurs (Fig. S17), which highlights the critical role of rGO in promoting the charge transfer and separation, thus providing additional evidence that [Ru(bpy)₃]²⁺ is adsorbed on the rGO nanosheets rather than the metal particles. Time-resolved PL decay spectroscopy was then employed to further reveal the charge dynamic behaviors. As depicted in Fig. 4d, all emission patterns of excited [Ru(bpy)₃]²⁺ aqueous solution in the absence or presence of catalysts follow one exponential decay [56]. Compared to blank [Ru(bpy)₃]²⁺ solution (210.1 ns), shortened PL lifetime can be observed in the presence of rGO (202.8 ns), rGO/Pd (196.9 ns), rGO/Pd@PtCu_{2L} (182.0 ns), rGO/Pd@PtCu_{6L} (189.1 ns), rGO/Pd@PtCu_{30L} (189.9 ns) and rGO/Pd@Pt₆L (188.0 ns), respectively (Table S3). The decline of PL lifetime follows the same sequence as the PL quenching degree, further evidencing more efficient suppression of detrimental charge recombination in rGO/Pd@PtCu_{2L} [17,57,58].

To gain an in-depth insight into the improved charge separation and transfer kinetics of rGO/Pd@PtCu_{2L}, electrochemical impedance spectroscopy (EIS) has been carried out to investigate the interfacial charge transfer resistance. As displayed in Fig. 4e, the Nyquist plot of rGO/Pd@PtCu_{2L} possesses the smallest arc radius among the different samples, revealing the lowest resistance for electron migration. Especially, the gradually reduced radii of Nyquist plots are observed when the thickness of PtCu shell decreases from 30 to 6 and then to 2 at. layers, disclosing the shell thickness dependent charge transfer kinetics. The above statements are further confirmed by the linear sweep voltammetry (LSV) curves examined with Ar-saturated KHCO₃ solution as electrolyte, from which it can be seen that rGO/Pd@PtCu_{2L} exhibits the highest current densities, signifying that the synergism of Pd core and ultrathin PtCu shell efficiently promotes the separation and transfer of charge carriers, thus accelerating the CO₂-to-CO/CH₄ conversion.

It should be noted that the shell thickness is not the only key variable influencing the efficiency of charge separation and migration. Particularly, with the same shell thickness, the larger current density of rGO/Pd@Pt₆L over that of rGO/Pd@PtCu_{6L} together with the smaller Nyquist arc and higher PL quenching degree validates that pure Pt shell is more conducive to smooth electron movement relative to PtCu shell. To further decipher the charge migration processes, density functional theory (DFT) simulations were performed to evaluate the electron flow behavior in detail. According to the aforementioned HRTEM results, Pd(100), Pt(100) and PtCu(100) facets are the most predominantly exposed crystallographic planes for rGO/Pd, rGO/Pd@Pt and rGO/Pd@PtCu samples, respectively, which were selected as the model surfaces to ensure the consistency of the theoretical models and the experimental results. According to the electrostatic potential, the work functions of PtCu_{1L}, PtCu_{2L}, PtCu_{3L} and PtCu_{4L} were calculated to be 4.98, 5.37, 5.49 and 5.52 eV, which are basically higher than those of rGO (4.33 eV) and Pd(100) (5.26 eV), but lower than that of Pt(100) (5.63 eV) (Table S4). Therefore, it can be inferred that the Fermi level is in the order of rGO > Pd > PtCu > Pt. As it is well documented that electrons will flow from the material with higher Fermi level to that with lower one [59], one can rationally deduce that electrons on the Pd core

Fig. 5. (a) Schematic energy-level diagram showing the electron transfer from [Ru(bpy)₃]Cl₂ to rGO/Pd@PtCu_{2L} catalyst; (b) differential charge density determined by first-principles simulations illustrating the electron distribution between Pd(100) substrate and PtCu(100) shell when the PtCu shell thickness is altered from 1 to 4 layers. The Pd, Pt and Cu atoms are marked in green, gray and blue, respectively. The olive and cyan colors represent an increase and decrease in electron density, respectively.

will migrate to the PtCu (or Pt) shell with more than one-layer thickness. This redistribution of charge is further revealed by experimental XPS results, implying the electron movement between the interfacial materials (Fig. 2g–i). Furthermore, valence-band XPS spectra manifest that the energy difference between the valence band (VB) edge and Fermi level is nearly zero for the rGO based samples, evidencing that the introduction of Pd core and PtCu (or Pt) shell does not alter the zero-bandgap feature of rGO (Fig. S18).

Considering that the highest occupied molecular orbital (HOMO) of [Ru(bpy)₃]Cl₂ is at 3.19 eV and its lowest unoccupied molecular orbital (LUMO) is at 5.68 eV relative to the vacuum level according to previous works [60,61], the Fermi levels of rGO, Pd, PtCu and Pt are lower than the LUMO of [Ru(bpy)₃]Cl₂ so that the photoexcited electrons in the LUMO of the light absorber can be transferred to the Fermi levels of them. The photogenerated electrons are preferentially transferred from [Ru(bpy)₃]Cl₂ to rGO through π - π interfacial interaction between them, which subsequently migrate to Pd cores and then to PtCu (or Pt) shells in larger work functions for CO₂ reduction (Fig. 5a). Owing to the higher work function of Pt compared to that of PtCu, the larger work function difference between Pd and Pt produces an enlarged driving force for promoted interfacial electron transfer from core to shell, well explaining the smoother charge separation and migration in rGO/Pd@Pt₆L relative to rGO/Pd@PtCu_{6L}.

Then the question comes up to reveal the role of PtCu thickness on the charge separation and transfer for the rGO/Pd@PtCu samples with the same exposed facets of PtCu(100). To investigate this mechanism, the interfacial models of Pd(100)@PtCu_{nL} with one to four atomic layers were established and the corresponding charge analyses were performed to track the charge migration behavior. As depicted in Fig. 5b, driving by the work function difference, electrons will flow from Pd to PtCu when two materials are combined together. That is, electrons could be accumulated on the upper PtCu shells. Moreover, according to the Bader charge analysis, this electron accumulation will experience a gradual decline as the PtCu thickness increases from one to four layers (Table S5), which can be clearly visualized from the differential charge density in Fig. 5b. The thickness-dependent charge separation will lead to the variation of the interfacial polarization [62], which could further contribute to the robust electron trapping ability of Pd@PtCu shells with lower-layer PtCu and thus facilitating the CO₂-to-CH₄ conversion efficiency. It is worth noting that the plasmonic absorption band of Pd, Pd@Pt and Pd@PtCu is located in UV region (Fig. S19), and the contribution of localized surface plasmon resonance (LSPR) on the charge transfer/separation can be ruled out [63–67].

In addition to the charge separation and transfer, the ultimate photocatalytic property is also correlated with the surface reactivity of the catalysts. As discussed before, despite the superior electron separation/transfer behavior, the activity and selectivity of rGO/Pd@Pt₆L in CH₄ production are much lower as compared with those of rGO/Pd@PtCu_{6L}, implying that the shell thickness dependent charge kinetics is not the only key factor determining the eventual photocatalytic performance. PtCu surface may provide more favorable reaction sites for CO₂-to-CH₄

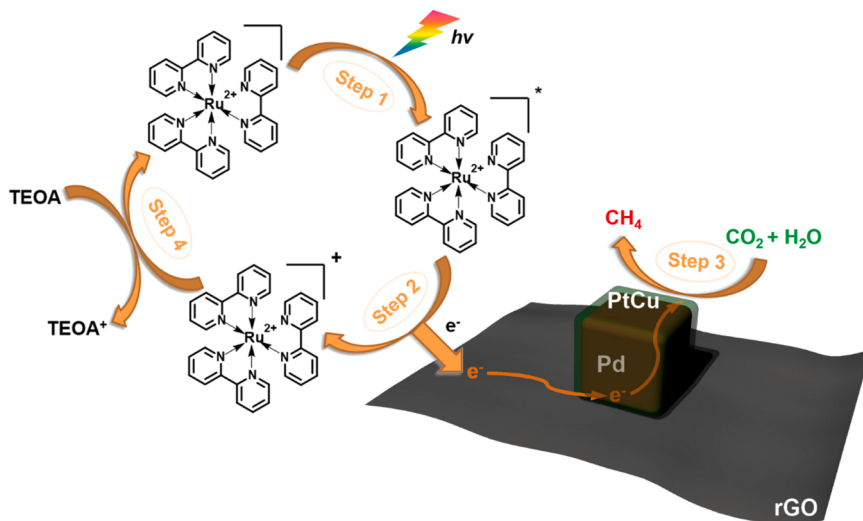
Table 1Optimized geometries for the adsorption of CO₂ and H₂O molecules on different metal surface and the corresponding lowest adsorption energy.

Model	Most stable CO ₂ adsorption configuration	E_{adCO_2} (eV)	Most stable H ₂ O adsorption configuration	E_{adH_2O} (eV)
Pd(100)		-0.02		-0.28
Pt(100)		-0.04		-0.29
PtCu(100) _{1L}		-0.92		-0.85
PtCu(100) _{2L}		-0.70		-0.61
PtCu(100) _{3L}		-0.59		-0.86
PtCu(100) _{4L}		-0.27		-0.70

conversion compared to Pt surface. According to the CO₂ temperature-programmed desorption (CO₂-TPD) profiles of rGO/Pd, rGO/Pd@Pt₆L and rGO/Pd@PtCu₆L samples, the peak at around 100 °C can be assigned to physisorbed CO₂, while another peak at around 500–600 °C originates from the chemisorbed CO₂ (Fig. S20). The desorption peak intensity of rGO/Pd@PtCu₆L at high temperature is much higher than those of rGO/Pd and rGO/Pd@Pt₆L, proving the better CO₂ adsorption on the PtCu(100) surface. Moreover, as demonstrated by the LSV curves conducted in Ar-saturated and CO₂-saturated 0.5 M KHCO₃ electrolyte, respectively, the higher current densities under CO₂ atmosphere compared to those under Ar bubbling can be assigned to the cathodic current generated by CO₂ reduction. As shown in Fig. 4f, rGO/Pd@PtCu₆L exhibits a larger current density enhancement as compared with rGO/Pd and rGO/Pd@Pt₆L, confirming that the PtCu(100) surface is more active for CO₂ reduction compared to Pd(100) and Pt(100) surface. Moreover, larger difference in the current density between Ar and CO₂ can be observed for rGO/Pd@PtCu₂L compared to those for rGO/Pd@PtCu₆L and rGO/Pd@PtCu₃₀L, meaning that the surface reactivity of PtCu(100) is also negatively correlative to the thickness of the shell.

To gain a deep insight into the influence of PtCu thickness on the surface reaction, the chemisorption behavior of CO₂ and H₂O molecules on the Pd, Pt and PtCu surfaces was further described by the DFT

calculations. As illustrated in Table 1, one can clearly see that PtCu surface exhibits much more negative CO₂ adsorption energies (ranging from -0.27 to -0.92 eV) when compared with those of Pd(100) (-0.02 eV) and Pt(100) (-0.04 eV), implying the substantially enhanced interaction between CO₂ molecules and PtCu surface. Additionally, as the thickness of PtCu increases from 1 to 4 at. layers, the adsorption energy of CO₂ experiences a gradual decline from -0.92 to -0.70 eV, and then to -0.59 and -0.27 eV, which suggests the steadily weakened CO₂ interaction. This shell-thickness dependence of CO₂ adsorption can be rationally ascribed to the synergistic interplay of surface strain and interfacial polarization [68,69]. Interestingly, a more favorable CO₂ adsorption can be expected on the surface of PtCu₁L and PtCu₂L with higher binding strength relative to H₂O molecules. In stark contrast, when compared to the CO₂ adsorption energies (E_{adCO_2}), the corresponding H₂O adsorption energies (E_{adH_2O}) on the Pd and Pt surface are much more negative, evincing a dominant proton reduction pathway. When the PtCu shell is thin enough, it is also possible that a two-step cascade catalytic process occurs, including the CO₂-to-CO conversion on Pd core and the further CO-to-CH₄ conversion on PtCu shell [70,71]. Taken together, the PtCu shell with lower atomic thickness promotes both the charge separation and the targeted reactant adsorption, thus accelerating the CO₂ reduction reaction and simultaneously restraining the side H₂ evolution reaction.



Scheme 1. Schematic process for the photocatalytic reduction of CO_2 to CH_4 using $[\text{Ru}(\text{bpy})_3]\text{Cl}_2$ as the photosensitizer and rGO/Pd@PtCu₂L as the catalyst.

Based on above analyses, a tentative mechanism for the photocatalytic CO_2 reduction over rGO/Pd@PtCu₂L is proposed. As illustrated in **Scheme 1**, under visible light irradiation, the electrons in the HOMO of the light absorber $[\text{Ru}(\text{bpy})_3]^{2+}$ are excited to the LUMO, and the $[\text{Ru}(\text{bpy})_3]^{2+}$ is promoted to the excited state by the photogenerated holes left in the HOMO (Step 1). This excited state is then reductively quenched by rGO/Pd@PtCu₂L to form an oxidized photosensitizer $[\text{Ru}(\text{bpy})_3]^{3+}$, during which the photoexcited electrons are transferred to rGO nanosheets owing to the $\pi-\pi$ interaction between them (Step 2). The transferred electrons then shift to the active sites on the surface of ultrathin PtCu shell with Pd core as the conducting channel [21]. The interfacial charge polarization promotes the electron transfer from Pd core to PtCu shell, causing the higher electron density on the PtCu surface. Moreover, the electron accumulation together with the compressive strain on the ultrathin PtCu surface strengthens the adsorption of CO_2 molecules, selectively promoting the 8-electron reduction of CO_2 to CH_4 when compared with the 2-electron reduction to CO and H_2 (Step 3). The oxidized $[\text{Ru}(\text{bpy})_3]^{3+}$ is then reduced back to $[\text{Ru}(\text{bpy})_3]^{2+}$ by the sacrificial electron donor TEOA to form an entire photoredox cycle (Step 4).

4. Conclusions

In summary, a stacking design of rGO/Pd@PtCu with atomically thin PtCu shell have been developed for photocatalytic reduction of CO_2 to CH_4 with remarkable activity, selectivity, and stability. In the smart design, rGO supporter and Pd core facilitate the separation and transfer of photo-created charge carriers from excited $[\text{Ru}(\text{bpy})_3]^{2+}$, while ultrathin PtCu shell provides highly active and selective sites for the CO_2 -to- CH_4 conversion. The combination of experimental analyses and theoretical simulations discloses that both the charge kinetics and surface reactivity of the ternary photocatalyst are dependent on the PtCu shell thickness, and the highest activity and selectivity in CH_4 production are achieved by shrinking the shell to two-atomic-layer thickness. On one hand, the strengthened Pd-PtCu interfacial charge polarization promotes the flow of photoelectrons from Pd core to PtCu shell, giving rise to more efficient charge separation and transfer. On the other hand, the increased electron density and compressive strain ameliorate the CO_2 adsorption on the PtCu surface, endowing the catalyst with enhanced activity and selectivity. We anticipate that this work would offer a “one stone two birds” design to simultaneously manipulate the interfacial charge transfer and surface catalytic reactivity for significantly enhanced photocatalytic CO_2 reduction by regulating the shell thickness of the well-designed catalyst.

CRediT authorship contribution statement

Yamin Xi: Conceptualization, Investigation, Data curation, Writing – original draft. **Yue Zhang:** Software, Formal analysis, Validation, Writing – original draft. **Xiaotong Cai:** Conceptualization, Investigation, Data curation. **Zhixin Fan:** Investigation. **Kefeng Wang:** Data curation. **Wenrou Dong:** Investigation. **Yue Shen:** Data curation. **Shuxian Zhong:** Validation, Investigation, Resources. **Li Yang:** Formal analysis, Supervision, Writing – review & editing, Funding acquisition, Project administration. **Song Bai:** Conceptualization, Formal analysis, Supervision, Writing – review & editing, Funding acquisition, Project administration.

Declaration of Competing Interest

The authors declare that they have no known competing financial interests or personal relationships that could have appeared to influence the work reported in this paper.

Acknowledgements

This work was financially supported by the National Natural Science Foundation of China (No. 21603191 and 21803063), Zhejiang Provincial Natural Science Foundation of China (No. LY20B030003 and LQ16B010001), Public Welfare Technology Application Research Plan Project of Zhejiang Province (Analysis Test Item, No. 2017C37024), Foundation of Science and Technology Bureau of Jinhua (No. 20204185), Self-Topic Fund of Zhejiang Normal University (2020ZS04) and Open Research Fund of Key Laboratory of the Ministry of Education for Advanced Catalysis Materials and Zhejiang Key Laboratory for Reactive Chemistry on Solid Surfaces, Zhejiang Normal University.

Appendix A. Supporting information

Supplementary data associated with this article can be found in the online version at doi:10.1016/j.apcatb.2022.121069.

References

- [1] S.C. Roy, O.K. Varghese, M. Paulose, C.A. Grimes, Toward solar fuels: photocatalytic conversion of carbon dioxide to hydrocarbons, *ACS Nano* 4 (2010) 1259–1278, <https://doi.org/10.1021/nn9015423>.
- [2] W. Tu, Y. Zhou, Z. Zou, Photocatalytic conversion of CO_2 into renewable hydrocarbon fuels: State-of-the-art accomplishment, challenges, and prospects, *Adv. Mater.* 26 (2014) 4607–4626, <https://doi.org/10.1002/adma.201400087>.

- [3] K. Li, B. Peng, T. Peng, Recent advances in heterogeneous photocatalytic CO₂ conversion to solar fuels, *ACS Catal.* 6 (2016) 7485–7527, <https://doi.org/10.1021/acscatal.6b02089>.
- [4] T. Kong, Y. Jiang, Y. Xiong, Photocatalytic CO₂ conversion: what can we learn from conventional CO_x hydrogenation? *Chem. Soc. Rev.* 49 (2020) 6579–6591, <https://doi.org/10.1039/C9CS00920e>.
- [5] F. Ren, W. Luo, Z. Zou, Near 100% selectivity for visible-light CO₂ reduction to CH₄ mediated by dual-metal sites in atomically-thin layers, *Sci. China Chem.* 62 (2019) 1553–1554, <https://doi.org/10.1007/s11426-019-9592-3>.
- [6] Z. Sun, N. Talreja, H. Tao, J. Texter, M. Muhler, J. Strunk, J. Chen, Catalysis of carbon dioxide photoreduction on nanosheets: Fundamentals and challenges, *Angew. Chem. Int. Ed.* 57 (2018) 7610–7627, <https://doi.org/10.1002/anie.201710509>.
- [7] S. Bai, J. Jiang, Q. Zhang, Y. Xiong, Steering charge kinetics in photocatalysis: Intersection of materials syntheses, characterization techniques and theoretical simulations, *Chem. Soc. Rev.* 44 (2015) 2893–2939, <https://doi.org/10.1039/C5CS00064e>.
- [8] H. Tong, S. Ouyang, Y. Bi, N. Umezawa, M. Oshikiri, J. Ye, Nano-photocatalytic materials: possibilities and challenges, *Adv. Mater.* 24 (2012) 229–251, <https://doi.org/10.1002/adma.201102752>.
- [9] S.N. Habichtreuter, L. Schmidt-Mende, J.K. Stolarczyk, Photocatalytic reduction of CO₂ on TiO₂ and other semiconductors, *Angew. Chem. Int. Ed.* 52 (2013) 7372–7408, <https://doi.org/10.1002/anie.201207199>.
- [10] M. Marszewski, S. Cao, J. Yu, M. Jaroniec, Semiconductor-based photocatalytic CO₂ conversion, *Mater. Horiz.* 2 (2015) 261–278, <https://doi.org/10.1039/c4mh00176a>.
- [11] H.L. Wu, X.B. Li, C.H. Tung, L.Z. Wu, Semiconductor quantum dots: an emerging candidate for CO₂ photoreduction, *Adv. Mater.* 31 (2019), 1900709, <https://doi.org/10.1002/adma.201900709>.
- [12] A. Dhakshinamoorthy, S. Navalon, A. Corma, H. Garcia, Photocatalytic CO₂ reduction by TiO₂ and related titanium containing solids, *Energy Environ. Sci.* 5 (2012) 9217–9233, <https://doi.org/10.1039/c2ee21948d>.
- [13] L. Bai, F. Ye, L. Li, J. Lu, S. Zhong, S. Bai, Facet engineered interface design of plasmonic metal and cocatalyst on BiOCl nanoplates for enhanced visible photocatalytic oxygen evolution, *Small* 13 (2017), 1701607, <https://doi.org/10.1002/smll.201701607>.
- [14] Y. Xu, A. Li, T. Yao, C. Ma, X. Zhang, J.H. Shah, H. Han, Strategies for efficient charge separation and transfer in artificial photosynthesis of solar fuels, *ChemSusChem* 10 (2017) 4277–4305, <https://doi.org/10.1002/cssc.201701598>.
- [15] Y. Zhang, B. Xia, J. Ran, K. Davey, S.Z. Qiao, Atomic-level reactive sites for semiconductor-based photocatalytic CO₂ reduction, *Adv. Energy Mater.* 3 (2020), 1903879, <https://doi.org/10.1002/aenm.201903879>.
- [16] X. Zhang, D. Luo, W. Zhang, W. Gao, X. Ning, H. Liu, B. Tian, B. Yang, G. Lu, Inhibition of hydrogen and oxygen recombination over amide-functionalized graphene and the enhancement of photocatalytic hydrogen generation in dye-sensitized AF-RGO/Pt photocatalyst dispersion, *Appl. Catal. B: Environ.* 232 (2018) 371–383, <https://doi.org/10.1016/j.apcatb.2018.03.070>.
- [17] C. Gao, S. Chen, Y. Wang, J. Wang, X. Zheng, J. Zhu, W. Zhang, Y. Xiong, Heterogeneous single-atom catalyst for visible-light-driven high-turnover CO₂ reduction: the role of electron transfer, *Adv. Mater.* 30 (2018), 1704624, <https://doi.org/10.1002/adma.201704624>.
- [18] U. Maitra, U. Gupta, M. De, R. Datta, A. Govindaraj, C.N.R. Rao, Highly effective visible-light-induced H₂ generation by single-layer 1T-MoS₂ and a nanocomposite of few-layer 2H-MoS₂ with heavily nitrogenated graphene, *Angew. Chem. Int. Ed.* 52 (2013) 13057–13061, <https://doi.org/10.1002/anie.201306918>.
- [19] C. Kong, S. Min, G. Lu, Dye-sensitized NiS_x catalyst decorated on graphene for highly efficient reduction of water to hydrogen under visible light irradiation, *ACS Catal.* 4 (2014) 2763–2769, <https://doi.org/10.1021/cs5006844>.
- [20] L. Tan, S.M. Xu, Z. Wang, Y. Xu, X. Wang, X. Hao, S. Bai, C. Ning, Y. Wang, W. Zhang, Y.K. Jo, S.J. Hwang, X. Cao, X. Zheng, H. Yan, Y. Zhao, H. Duan, Y. F. Song, Highly selective photoreduction of CO₂ with suppressing H₂ evolution over monolayered double hydroxide under irradiation above 600 nm, *Angew. Chem. Int. Ed.* 58 (2019) 11860–11867, <https://doi.org/10.1002/anie.201904246>.
- [21] S. Zhong, Y. Xi, Q. Chen, J. Chen, S. Bai, Bridge engineering in photocatalysis and photoelectrocatalysis, *Nanoscale* 12 (2020) 5764–5791, <https://doi.org/10.1039/c9nr10511e>.
- [22] X. Li, J. Yu, M. Jaroniec, X. Chen, Cocatalysts for selective photoreduction of CO₂ into solar fuels, *Chem. Rev.* 119 (2019) 3962–4179, <https://doi.org/10.1021/acs.chemrev.8b00400>.
- [23] J. Ran, M. Jaroniec, S.Z. Qiao, Cocatalysts in semiconductor-based photocatalytic CO₂ reduction: achievements, challenges, and opportunities, *Adv. Mater.* 30 (2018), 1704649, <https://doi.org/10.1002/adma.201704649>.
- [24] S. Zhong, Y. Xi, S. Wu, Q. Liu, L. Zhao, S. Bai, Hybrid cocatalysts in semiconductor-based photocatalysis and photoelectrocatalysis, *J. Mater. Chem. A* 8 (2020) 14863–14894, <https://doi.org/10.1039/d0ta04977h>.
- [25] S. Bai, W. Jiang, Z. Li, Y. Xiong, Surface and interface engineering in photocatalysis, *ChemNanoMat* 1 (2015) 223–239, <https://doi.org/10.1002/cnma.201500069>.
- [26] S. Bai, Y. Xiong, Some recent developments in surface and interface design for photocatalytic and electrocatalytic hybrid structures, *Chem. Commun.* 51 (2015) 10261–10271, <https://doi.org/10.1039/c5cc02704g>.
- [27] S. Bai, W. Yin, L. Wang, Z. Li, Y. Xiong, Surface and interface design in cocatalysts for photocatalytic water splitting and CO₂ reduction, *RSC Adv.* 6 (2016) 57446–57463, <https://doi.org/10.1039/c6ra10539d>.
- [28] Q. Xiang, B. Cheng, J. Yu, Graphene-based photocatalysts for solar-fuel generation, *Angew. Chem. Int. Ed.* 54 (2015) 11350–11366, <https://doi.org/10.1002/anie.201411096>.
- [29] M.Q. Yang, Y.J. Xu, Photocatalytic conversion of CO₂ over graphene-based composites: Current status and future perspective, *Nanoscale Horiz.* 1 (2016) 185–200, <https://doi.org/10.1039/c5nh00113g>.
- [30] G. Kresse, J. Furthmüller, Efficiency of ab-initio total energy calculations for metals and semiconductors using a plane-wave basis set, *J. Comput. Mater. Sci.* 6 (1996) 15–50, [https://doi.org/10.1016/0927-0256\(96\)00008-0](https://doi.org/10.1016/0927-0256(96)00008-0).
- [31] G. Kresse, D. Joubert, From ultrasoft pseudopotentials to the projector augmented-wave method, *Phys. Rev. B* 59 (1999) 1758–1775, <https://doi.org/10.1103/physrevb.59.1758>.
- [32] J.P. Perdew, K. Burke, M. Ernzerhof, Generalized gradient approximation made simple, *Phys. Rev. Lett.* 77 (1996) 3865–3868, <https://doi.org/10.1103/physrevlett.77.3865>.
- [33] S. Bai, J. Ge, L. Wang, M. Gong, M. Deng, Q. Kong, L. Song, J. Jiang, Q. Zhang, Y. Luo, Y. Xie, Y. Xiong, A unique semiconductor-metal-graphene stack design to harness charge flow for photocatalysis, *Adv. Mater.* 26 (2014) 5689–5695, <https://doi.org/10.1002/adma.201401817>.
- [34] B. Lim, M. Jiang, J. Tao, P.H.C. Camargo, Y. Zhu, Y. Xia, Shape-controlled synthesis of Pd nanocrystals in aqueous solutions, *Adv. Funct. Mater.* 19 (2009) 189–200, <https://doi.org/10.1002/adfm.200801439>.
- [35] Z. Xia, S. Guo, Strain engineering of metal-based nanomaterials for energy electrocatalysis, *Chem. Soc. Rev.* 48 (2019) 3265–3278, <https://doi.org/10.1039/c8cs00846a>.
- [36] J.S. Kim, H.K. Kim, S.H. Kim, I. Kim, T. Yu, G.H. Han, K.Y. Lee, J.C. Lee, J.P. Ahn, Catalytically active Au layers grown on Pd nanoparticles for direct synthesis of H₂O₂: Lattice strain and charge-transfer perspective analyses, *ACS Nano* 13 (2019) 4761–4770, <https://doi.org/10.1021/acsnano.9b01394>.
- [37] R.P. Janssonius, L.M. Reid, C.N. Virca, C.P. Berlinguette, Strain engineering electrocatalysts for selective CO₂ reduction, *ACS Energy Lett.* 4 (2019) 980–986, <https://doi.org/10.1021/acsenrgylett.9b00191>.
- [38] K. Spyrou, M. Calvaresi, E.K. Diamanti, T. Tsoufis, D. Gournis, P. Rudolf, F. Zerbetto, Graphite oxide and aromatic amines: Size matters, *Adv. Funct. Mater.* 25 (2015) 263–269, <https://doi.org/10.1002/adfm.201402622>.
- [39] Q. Liu, S. Wang, Q. Ren, T. Li, G. Tu, S. Zhong, Y. Zhao, S. Bai, Stacking design in photocatalysis: synergizing cocatalyst roles and anti-corrosion functions of metallic Mo₂S and graphene for remarkable hydrogen evolution over CdS, *J. Mater. Chem. A* 9 (2021) 1552–1562, <https://doi.org/10.1039/d0ta10255e>.
- [40] M. Gong, D. Xiao, Z. Deng, R. Zhang, W. Xia, T. Zhao, X. Liu, T. Shen, Y. Hu, Y. Lu, X. Zhao, H. Xin, D. Wang, Structure evolution of PtCu nanoframes from disordered to ordered for the oxygen reduction reaction, *Appl. Catal. B: Environ.* 282 (2021), 119617, <https://doi.org/10.1016/j.apcatb.2020.119617>.
- [41] X. Tian, X. Zhao, Y.Q. Su, L. Wang, H. Wang, D. Dang, B. Chi, H. Liu, E.J. M. Hensen, X.W. Lou, B.Y. Xia, Engineering bunched Pt-Ni alloy nanocages for efficient oxygen reduction in practical fuel cells, *Science* 366 (2019) 850–856, <https://doi.org/10.1126/science.aaw7493>.
- [42] K. Jiang, W.B. Cai, Carbon supported Pd-Pt-Cu nanocatalysts for formic acid electrooxidation: Synthetic screening and componential functions, *Appl. Catal. B: Environ.* 147 (2014) 185–192, <https://doi.org/10.1016/j.apcatb.2013.08.037>.
- [43] Y. Wei, Z. Zhao, J. Liu, S. Liu, C. Xu, A. Duan, G. Jiang, Multifunctional catalysts of three-dimensionally ordered macroporous oxide-supported Au@Pt core-shell nanoparticles with high catalytic activity and stability for soot oxidation, *J. Catal.* 317 (2014) 62–74, <https://doi.org/10.1016/j.jcat.2014.05.014>.
- [44] Z. Zheng, Y.H. Ng, D.W. Wang, R. Amal, Epitaxial growth of Au-Pt-Ni nanorods for direct high selectivity H₂O₂ production, *Adv. Mater.* 28 (2016) 9949–9955, <https://doi.org/10.1002/adma.201603662>.
- [45] Z.J. Fan, W. Kai, J. Yan, T. Wei, L.J. Zhi, J. Feng, Y.M. Ren, L.P. Song, F. Wei, Facile synthesis of graphene nanosheets via Fe reduction of exfoliated graphite oxide, *ACS Nano* 5 (2021) 1552–1562, <https://doi.org/10.1021/nn10239t>.
- [46] Z. Fan, K. Wang, T. Wei, J. Yan, L. Song, B. Shao, An environmentally friendly and efficient route for the reduction of graphene oxide by aluminum powder, *Carbon* 48 (2010) 1686–1689, <https://doi.org/10.1016/j.carbon.2009.12.063>.
- [47] N.E. Motl, E. Ewusi-Annan, I.T. Sines, L. Jensen, R.E. Schaak, Au-Cu alloy nanoparticles with tunable compositions and plasmonic properties: Experimental determination of composition and correlation with theory, *J. Phys. Chem. C* 114 (2010) 19263–19269, <https://doi.org/10.1021/jp107637j>.
- [48] J. Zhang, H. Yang, G. Shen, P. Cheng, J. Zhang, S. Guo, Reduction of graphene oxide via L-ascorbic acid, *Chem. Commun.* 46 (2010) 1112–1114, <https://doi.org/10.1039/b917705>.
- [49] C.K. Chua, A. Ambrosi, M. Pumera, Graphene oxide reduction by standard industrial reducing agent: thiourea dioxide, *J. Mater. Chem.* 22 (2012) 11054–11061, <https://doi.org/10.1039/c2jm16054d>.
- [50] J.W. Lee, T. Ahn, D. Soundararajan, J.M. Ko, J.D. Kim, Non-aqueous approach to the preparation of reduced graphene oxide/α-Ni(OH)₂ hybrid composites and their high capacitance behavior, *Chem. Commun.* 47 (2011) 6305–6307, <https://doi.org/10.1039/c1cc11566a>.
- [51] R. Xie, G. Fan, Q. Ma, L. Yang, F. Li, Facile synthesis and enhanced catalytic performance of graphene-supported Ni nanocatalyst from a layered double hydroxide-based composite precursor, *J. Mater. Chem. A* 2 (2014) 7880–7889, <https://doi.org/10.1039/c4ta00395k>.
- [52] Y. Xi, W. Chen, W. Dong, Z. Fan, K. Wang, Y. Shen, G. Tu, S. Zhong, S. Bai, Engineering interfacial facet of S-scheme heterojunction for improved photocatalytic hydrogen evolution by modulating the internal electric field, *ACS Appl. Mater. Interface* 13 (2021) 39491–39500, <https://doi.org/10.1021/acsmami.1c1233>.

- [53] Y. Xi, X. Zhang, Y. Shen, W. Dong, Z. Fan, K. Wang, S. Zhong, S. Bai, Aspect ratio dependent photocatalytic enhancement of CsPbBr₃ in CO₂ reduction with two-dimensional metal organic framework as a cocatalyst, *Appl. Catal. B Environ.* 297 (2021), 120411, <https://doi.org/10.1016/j.apcatb.2021.120411>.
- [54] Q. Chen, W. Mo, G. Yang, J. Chen, H. Lin, S. Bai, Significantly enhanced photocatalytic CO₂ reduction by surface amorphization of cocatalysts, *Small* 17 (2021), 2102105, <https://doi.org/10.1002/smll.202102105>.
- [55] Q. Liu, S. Wang, W. Mo, Y. Zheng, Y. Xu, G. Yang, S. Zhong, J. Ma, D. Liu, S. Bai, Emerging stacked photocatalyst design enables spatially separated Ni(OH)₂ redox cocatalysts for overall CO₂ reduction and H₂O oxidation, *Small* 18 (2022), 2104681, <https://doi.org/10.1002/smll.202104681>.
- [56] H.K. Wu, Y.H. Li, M.Y. Qi, Q. Lin, Y.J. Xu, Enhanced photocatalytic CO₂ reduction with suppressing H₂ evolution via Pt cocatalyst and surface SiO₂ coating, *Appl. Catal. B Environ.* 278 (2020), 119267, <https://doi.org/10.1016/j.apcatb.2020.119267>.
- [57] K.Q. Lu, Y.H. Li, F. Zhang, M.Y. Qi, X. Chen, Z.R. Tang, Y.M.A. Yamada, M. Anpo, M. Conte, Y.J. Xu, Rationally designed transition metal hydroxide nanosheet arrays on graphene for artificial CO₂ reduction, *Nat. Commun.* 11 (2020) 5181, <https://doi.org/10.1038/s41467-020-18944-1>.
- [58] J. Yang, Z. Wang, J. Jiang, W. Chen, F. Liao, X. Ge, X. Zhou, M. Chen, R. Li, Z. Xue, G. Wang, X. Duan, G. Zhang, Y.G. Wang, Y. Wu, In-situ polymerization induced atomically dispersed manganese sites as cocatalyst for CO₂ photoreduction into synthesis gas, *Nano Energy* 76 (2020), 105059, <https://doi.org/10.1016/j.nanoen.2020.105059>.
- [59] A. Kahn, Fermi level, work function and vacuum level, *Mater. Horiz.* 3 (2016) 7–10, <https://doi.org/10.1039/c5mh00160a>.
- [60] C. Gao, Q. Meng, K. Zhao, H. Yin, D. Wang, J. Guo, S. Zhao, L. Chang, M. He, Q. Li, H. Zhao, X. Huang, Y. Gao, Z. Tang, Co₃O₄ hexagonal platelets with controllable facets enabling highly efficient visible-light photocatalytic reduction of CO₂, *Adv. Mater.* 28 (2016) 6485–6490, <https://doi.org/10.1002/adma.201601387>.
- [61] K. Zhao, S. Zhao, C. Gao, J. Qi, H. Yin, D. Wei, M.F. Mideksa, X. Wang, Y. Gao, Z. Tang, R. Yu, Metallic cobalt-carbon composite as recyclable and robust magnetic photocatalyst for efficient CO₂ reduction, *Small* 14 (2018), 1800762, <https://doi.org/10.1002/smll.201800762>.
- [62] S. Bai, C. Wang, M. Deng, M. Gong, Y. Bai, J. Jiang, Y. Xiong, Surface polarization matters: enhancing the hydrogen-evolution reaction by shrinking Pt shells in Pt-Pd-graphene stack structures, *Angew. Chem. Int. Ed.* 53 (2014) 12120–12124, <https://doi.org/10.1002/anie.201406468>.
- [63] P. Christopher, H. Xin, A. Marimuthu, S. Linic, Singular characteristics and unique chemical bond activation mechanisms of photocatalytic reactions on plasmonic nanostructures, *Nat. Mater.* 11 (2012) 1044–1050, <https://doi.org/10.1038/nmat3454>.
- [64] U. Aslam, S. Chavez, S. Linic, Controlling energy flow in multimetallic nanostructures for plasmonic catalysis, *Nat. Nanotechnol.* 12 (2017) 1000–1005, <https://doi.org/10.1038/nano.2017.131>.
- [65] S. Chavez, U. Aslam, S. Linic, Design principles for directing energy and energetic charge flow in multicomponent plasmonic nanostructures, *ACS Energy Lett.* 3 (2018) 1590–1596, <https://doi.org/10.1021/acsenergylett.8b00841>.
- [66] L. Nguyen, M. Dass, M.F. Ober, L.V. Besteiro, Z.M. Wang, B. Nickel, A.O. Govorov, T. Liedl, A. Heuer-Jungemann, Chiral assembly of gold-silver core-shell plasmonic nanorods on DNA origami with strong optical activity, *ACS Nano* 14 (2020) 7454–7461, <https://doi.org/10.1021/acsnano.0c03127>.
- [67] C. Langhammer, Z. Yuan, I. Zoric, B. Kasemo, Plasmonic properties of supported Pt and Pd nanostructures, *Nano Lett.* 6 (2006) 833–838, <https://doi.org/10.1021/nl060219x>.
- [68] S. Bai, L. Yang, C. Wang, Y. Lin, J. Lu, J. Jiang, Y. Xiong, Boosting photocatalytic water splitting: interfacial charge polarization in atomically controlled core-shell cocatalysts, *Angew. Chem. Int. Ed.* 54 (2015) 14810–14814, <https://doi.org/10.1002/anie.201508024>.
- [69] X. Cai, F. Wang, R. Wang, Y. Xi, A. Wang, J. Wang, B. Teng, S. Bai, Synergism of surface strain and interfacial polarization on Pd@Au core-shell cocatalysts for highly efficient photocatalytic CO₂ reduction over TiO₂, *J. Mater. Chem. A* 8 (2020) 7350–7359, <https://doi.org/10.1039/d0ta01247e>.
- [70] Gurudayal, D. Perone, S. Malani, Y. Lum, S. Haussener, J.W. Ager, Sequential cascade electrocatalytic conversion of carbon dioxide to C-C coupled products, *ACS Appl. Energy Mater.* 2 (2019) 4551–4559, <https://doi.org/10.1021/acsaeem.9b00791>.
- [71] I. Shown, H.C. Hsu, Y.C. Chang, C.H. Lin, P.K. Roy, A. Ganguly, C.H. Wang, J. K. Chang, C. Wu, L.C. Chen, K.H. Chen, Highly efficient visible light photocatalytic reduction of CO₂ to hydrocarbon fuels by Cu-nanoparticle decorated graphene oxide, *Nano Lett.* 14 (2014) 6097–6103, <https://doi.org/10.1021/nl503609v>.